Nano-Micro Letters

e-ISSN 2150-5551
CN 31-2103/TB

ARTICLE

https://doi.org/10.1007/s40820-026-02211-x

Cite as
Nano-Micro Lett.
(2026) 18:404

Received: 14 January 2026
Accepted: 7 April 2026

Engineering Fe–Ni Dual-Atom Sites Via Ru Nanoclusters on 3D Carbon Aerogel for Enhanced Bifunctional Oxygen Electrocatalysis

Yifan Zhang[1], Kexin Kong[1], Hongyuan Jie[2], Xiaoyan Jin[3], Long Tian[4], Yipu Liu[2], Zhijuan Pan[1], Seong-Ju Hwang[5] ✉, Liang Li[6] ✉, Zhe Wang[1] ✉

HIGHLIGHTS

- A heterogeneous catalyst consisting of atomically dispersed FeN_4 and NiN_4 sites along with Ru_6 nanoclusters anchored on a 3D carbon aerogel was synthesized.
- The Ru_6 nanoclusters optimize the electron transfer from the Fe/Ni centers to the key intermediate (*OH) at the rate-determining steps.
- Zin–air battery employed FeN_4–Ru_6–NiN_4@PCA as the air cathode catalysts achieves an exceptional long-term cycling stability for over 2000 h.

ABSTRACT Dual-atom catalysts (DACs) show great promise in catalyzing oxygen reduction/evolution reactions (ORR/OER), yet facing significant challenges in achieving simultaneous high catalytic activity and stability in zinc–air batteries (ZABs). In this study, we synthesized a porous three-dimensional carbon aerogel anchored with atomically isolated FeN_4/NiN_4 dual sites and Ru_6 nanoclusters (FeN_4–Ru_6–NiN_4@PCA) to address these challenges. The adjacent Ru_6 nanoclusters effectively regulate the geometric structures of FeN_4 and NiN_4 sites and catalyze the formation of a highly graphitic carbon matrix. These structural features endow FeN_4–Ru_6–NiN_4@PCA with remarkable ORR/OER activity and stability, outperforming counterparts with only FeN_4/NiN_4 dual species and benchmark Pt/C and RuO_2 catalysts. Density functional theory calculations reveal that Ru6 clusters induce obvious electron redistribution of FeN_4/NiN_4 sites and optimize their electron transfer to the key oxygen intermediates (OH*) at the rate-determining steps, thereby accelerating the ORR and OER kinetics. When employed FeN_4–Ru_6–NiN_4@PCA as the cathode catalyst in ZABs, the resulting ZAB delivers a peak power density of 197.76 mW cm^{-2} and demonstrates outstanding cycling stability over 2000 h, highlighting its great potential for use in applications of energy storage device.

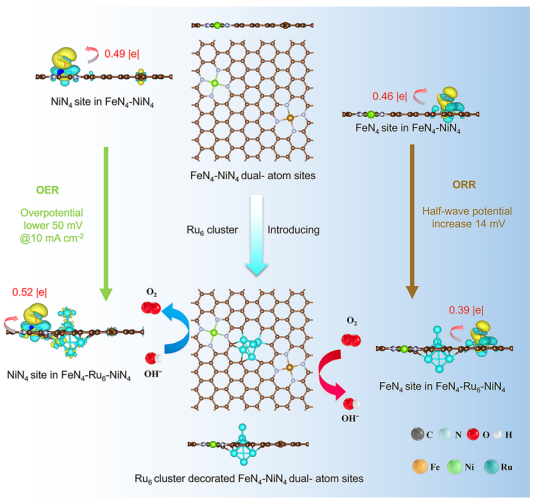

KEYWORDS Dual-atom catalysts; Nanoclusters; Porous carbon aerogels; ORR/OER; Zinc–air batteries

✉ Seong-Ju Hwang, hwangsju@yonsei.ac.kr; Liang Li, lli@suda.edu.cn; Zhe Wang, zhewang1119@suda.edu.cn

[1] College of Textile and Clothing Engineering, National Engineering Laboratory for Modern Silk, Soochow University, Suzhou 215123, People's Republic of China

[2] State Key Laboratory of Marine Resource Utilization in South China Sea, School of Materials Science and Engineering, Hainan University, Haikou 570228, People's Republic of China

[3] Department of Applied Chemistry, University of Seoul, Seoul 02504, Republic of Korea

[4] Newtech Textile Technology Development (Shanghai) Co., Ltd., Shanghai 201506, People's Republic of China

[5] Department of Materials Science and Engineering, Yonsei University, Seoul 03722, Republic of Korea

[6] School of Physical Science and Technology, Jiangsu Key Laboratory of Frontier Material Physics and Devices, Suzhou Key Laboratory of Intelligent Photoelectric Perception, Jiangsu Key Laboratory of Advanced Negative Carbon Technologies, Center for Energy Conversion Materials & Physics (CECMP), Soochow University, Suzhou 215006, People's Republic of China

Published online: 18 June 2026

Shanghai Jiao Tong University Press

Springer

1 Introduction

The development of efficient renewable energy storage and conversion technologies is essential for addressing the global energy crisis and climate change. Zinc–air batteries (ZABs) have received significant attention owing to their high theoretical energy density, safety features, and economic advantage[1–4]. However, practical implementation faces challenges from the slow kinetics of the oxygen reduction reaction/oxygen evolution reaction (ORR/OER), along with poor reversible stability at air electrodes [5–7]. These issues collectively result in low energy conversion efficiency and limited cycling life. Recently, single-atom catalysts (SACs) have sparked tremendous research activity as valuable alternatives to commercial Pt/C and RuO_2 catalysts for ORR/OER due to their adjustable electronic structures and high atomic utilization efficiency [3, 8–10]. However, SACs typically consist of only one type of metal active site, posing a significant challenge in achieving excellent catalyst functionality and durability for both the ORR and OER [11, 12].

Dual-atom catalysts (DACs) having two distinct metal active centers and various local configurations present a promising approach to address the limitations of SACs [9, 13–15]. DACs offer diverse active sites, adjustable local geometric structures (e.g., metal species, coordination environments, and spatial architectures), and potential synergistic effects between the metal sites [16, 17]. The structural flexibility of DACs enables precise optimization of the adsorption/desorption behavior of oxygen-containing intermediate species, thereby enhancing ORR and OER kinetics [18, 19]. Recent efforts have focused on developing carbon-supported DACs for bifunctional oxygen catalysis [20]. For instance, Tang et al. reported a Janus dual-atom catalyst on carbon nanosheets where Fe and Co sites were coordinated with N and O atoms, respectively. The strong interaction between the Fe–N_3 and Co–O_3 moieties can modulate the d-orbital energy level of the active metal atoms to optimize the binding energy of oxygenated intermediates and improving both ORR and OER performance [13].

In ZABs, alongside activity, stability is crucial for air cathode catalysts. Carbon-supported DACs often face challenges like metal leaching and carbon corrosion under high-voltage oxidizing conditions, particularly during high-current density charging [21–23]. Recent studies have shown that incorporating nanoclusters (NCs) or nanoparticles (NPs) into SACs/DACs on carbon substrates can notably enhance their electrochemical stability and corrosion resistance. In a prior study, a carbon fiber-supported DAC was developed with CoN_4–FeN_4 dual sites and Co_2Fe–Fe_5 nanoclusters coexisting. The synergy between the dual-atom sites and nanoclusters optimized the electronic structure of the metal active sites, reinforcing their interaction with the carbon supports [24, 25]. This optimization led to improved bifunctional oxygen catalytic activity and stability. However, most reported DACs only involve two types of metal species (e.g., A–B dual-atom sites with AB, A, or B clusters) due to challenges in precisely constructing dual-atom sites and nanoclusters with different metal species. To date, DACs combining A–B dual-atom sites with C-type nanoclusters (where C is a different metal) have been rarely documented, and their catalytic mechanism remains unexplored [26–28].

In this study, we synthesized a heterogeneous catalyst consisting of spatially separated FeN_4 and NiN_4 sites along with Ru_6 nanoclusters supported on a three-dimensional (3D) porous carbon aerogel (FeN_4–Ru_6–NiN_4@PCA). This catalyst exhibits outstanding bifunctional oxygen catalytic performance, with a half-wave potential of 0.874 V for the ORR and a potential of 1.58 V to reach a current density of 10 mA cm^{-2} for the OER. It surpassed not only catalysts containing only FeN_4/NiN_4 dual sites but also the benchmark materials Pt/C and RuO_2. Moreover, the heterogeneous catalyst exhibits superior stability in both ORR and OER. Density functional theory (DFT) calculations indicated that the Ru6 clusters induce obvious charge redistribution of FeN_4/NiN_4 sites and optimize the electron transfer from the Fe/Ni centers to the key intermediate (*OH) at the rate-determining steps, thereby improving the ORR and OER kinetics. Notably, ZABs utilizing FeN_4–Ru_6–NiN_4@PCA as the air cathode catalysts show a maximum power density of 197.76 mW cm^{-2} and sustained long-term cycling stability exceeding 2000 h (2000 cycles) [29]. Moreover, a system of three interconnected solid-state flexible ZABs successfully charged mobile phones and powered LED lights, showcasing significant promise for practical energy storage technologies.

2 Experimental Section

2.1 Materials

Carboxylated cellulose nanofibers (6 wt%) and ruthenium chloride hydrate ($RuCl_3 \cdot H_2O$, 98 wt%) were purchased

https://doi.org/10.1007/s40820-026-02211-x

from Shanghai Macklin Biochemical Co., Ltd. 2-Methylimidazole ($C_4H_6N_2$, 98 wt%), nickel nitrate hexahydrate ($Ni(NO_3)_2{\cdot}6H_2O$, 98 wt%) and zinc nitrate hexahydrate ($Zn(NO_3)_2{\cdot}6H_2O$, 99.99 wt%) were all purchased from Shanghai Aladdin Biochemical Technology Co., Ltd. Iron(III) nitrate nonahydrate ($Fe(NO_3)_3{\cdot}9H_2O$, 99.99 wt%) was purchased from Shanghai Acmec Biochemical Technology Co., Ltd. Graphene oxide (GO, 2 wt%) was purchased from Newtech Textile Technology Development (Shanghai) Co., Ltd..

2.2 Synthesis of FeN_4-Ru_6-NiN_4@PCA

2.2.1 Synthesis of Fe-ZIF@CNF

Five grams of carboxylated cellulose solution was dispersed in 10 g of deionized (DI) water and stirred with a magnetic stirrer to obtain a homogeneous dispersion. Subsequently, 0.1 g of zinc nitrate hexahydrate ($Zn(NO_3)_2{\cdot}6H_2O$) and 6.7 mg of iron nitrate hexahydrate ($Fe(NO_3)_3{\cdot}6H_2O$) (with a mass ratio of) were added into above dispersion, followed by stirring for 30 min, to form solution A. Separately, 1.6 g of 2-methylimidazole was dissolved in 15 g of DI water under magnetic stirring for 30 min, denoted as Solution B. Solution B was then poured into Solution A and stirred for 4 h. The mixture was centrifuge and washed with DI water to collect a pale-yellow product, denoted as Fe-ZIF@CNF.

2.2.2 Synthesis of NiRu@GO

0.3125 g of 2 wt% aqueous dispersion of graphene oxide (GO) was added in 15 g of DI water and subjected to low-temperature sonication with stirring. 4.2 mg of $Ni(NO_3)_2{\cdot}6H_2O$ and 1.7 mg of $RuCl_3{\cdot}H_2O$ was then dissolved in above solution, followed by low-temperature stirring and sonication for 1 h, yielding NiRu@GO.

2.2.3 Synthesis of FeN_4-Ru_6-NiN_4@PCA

The as-prepared Fe-ZIF@CNF was added into the NiRu@GO solution and stirred for 30 min to achieve a uniform mixture. The composite was then subjected to directional freeze-drying, resulting in the Fe-ZIF@CNF/NiRu@GO aerogel. The aerogel was transferred to a tube furnace for a two-step heat treatment under a flowing argon (Ar) atmosphere. The pyrolysis procedure was as following: The aerogel was firstly stabilized by heating from room temperature to 550 °C at 2 °C min^{-1}, followed by a 2—h hold and then suffered from the carbonization treatment by heating from 550 to 920 °C at 5 °C min^{-1}, followed by another 2 h hold. The final product was denoted as FeN_4-Ru_6-NiN_4@PCA.

For comparison, reference samples including PCA, FeN_4@PCA, and FeN_4-NiN_4@PCA were prepared using identical procedures. PCA was synthesized without adding any metal species, FeN_4@PCA was prepared with only iron addition, and FeN_4-NiN_4@PCA was obtained with only iron and nickel species additions.

3 Results and Discussion

3.1 Morphological, Structural, and Electronic Features of FeN_4–Ru_6–NiN_4@PCA

Figure 1a shows the synthesis process of FeN_4–Ru_6–NiN_4@PCA. Atomically isolated dual NiN_4/FeN_4 sites accompanied with adjacent Ru_6 NCs were stabilized on a porous 3D carbon aerogel through freeze-drying and subsequent pyrolysis. Initially, hydroxy cellulose fibers are dispersed in deionized water, followed by the addition of zinc nitrate and ferric nitrate to create a uniform solution. A 2-methylimidazole solution was then introduced, and the mixture was stirred for 4 h [30]. Subsequently, aqueous solutions containing Ni, Ru, and graphene oxide (GO) were added with continuous stirring. The resulting mixture underwent directional freeze-drying for 48 h to yield the FeNiRu-ZIF-8/GO/CNF aerogel. Finally, the aerogel was pyrolyzed under flowing Ar to form a 3D porous honeycomb structure (Fig. S1). During pyrolysis, cellulose fibers acted as the "skeleton," and GO served as "cement," transforming into carbon fibers and graphene, respectively. ZIFs converted into porous carbon nanocages entwined with carbon nanotubes (CNTs), collectively forming the porous carbon matrix [31]. Meanwhile, Fe and Ni species transitioned into well-dispersed NiN_4 and FeN_4 sites, respectively, and Ru species were reduced to form Ru_6 NCs [32].

Scanning electron microscopy (SEM) images of FeN_4–Ru_6–NiN_4@PCA (Fig. 1b) reveal a 3D honeycomb network structure with interconnected directional walls forming a highly porous matrix. Transmission electron microscopy (TEM) analysis was also conducted, as shown

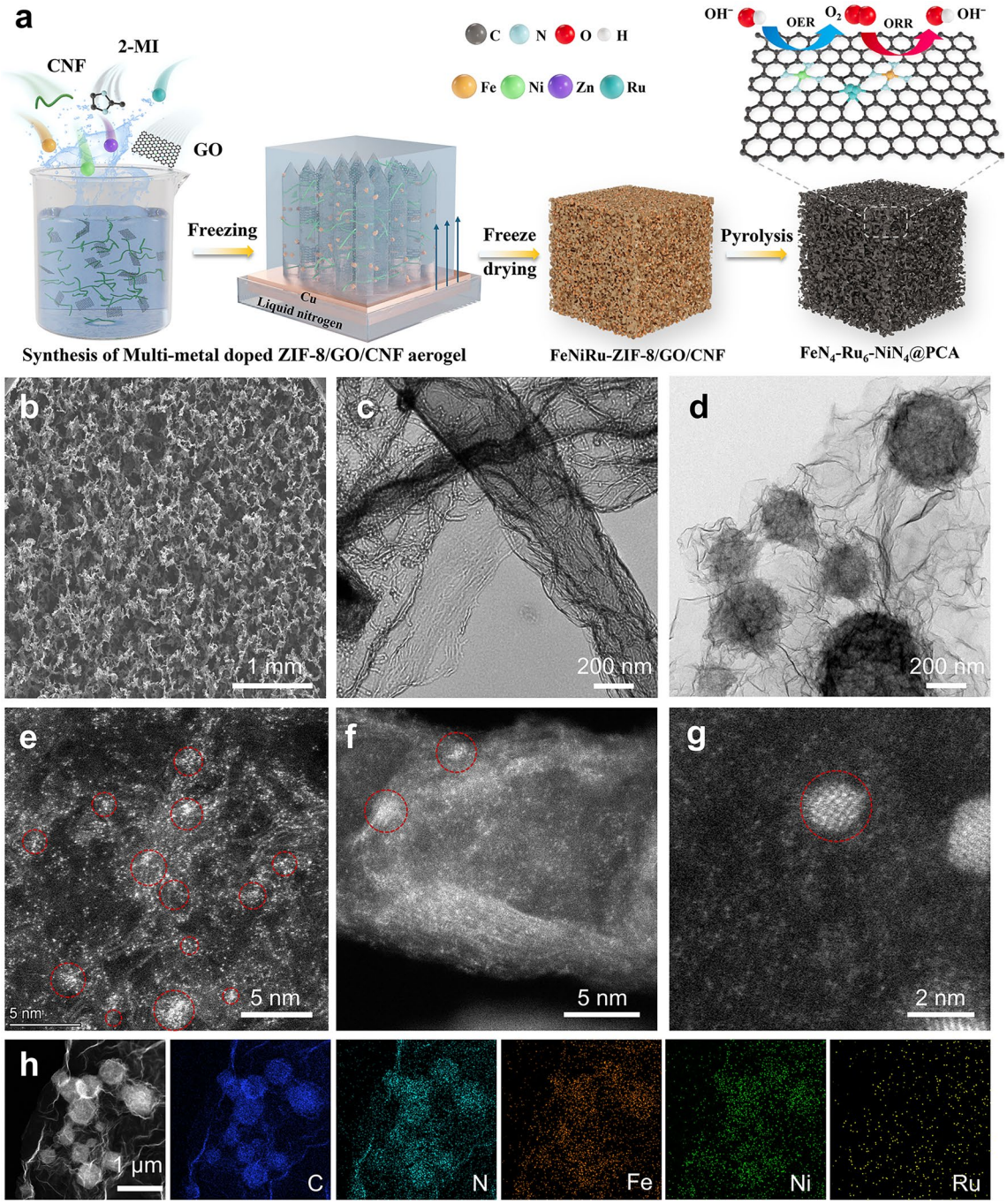

Fig. 1 Morphology and structure of FeN_4–Ru_6–NiN_4@PCA. **a** Synthetic procedure of the porous carbon aerogel with dual-atom NiN_4/FeN_4 sites and Ru_6 NCs. **b** SEM, **c, d** TEM, and **e–g** AC-STEM images of FeN_4–Ru_6–NiN_4@PCA. **h** HAADF-TEM image and EDS-elemental mapping data of FeN_4–Ru_6–NiN_4@PCA

in Figs. 1c, d, and S2; FeN_4–Ru_6–NiN_4@PCA exhibited a hierarchical structure, where MOF-derived porous carbon spheres, cellulose-derived carbon fibers, and several CNTs were loaded onto the reduced graphene oxide (rGO) sheet [33, 34]. Additionally, small nanoparticles are visible on the rGO sheets. N_2 adsorption–desorption isotherm measurements were performed for FeN_4–Ru_6–NiN_4@PCA to evaluate their Brunauer–Emmett–Teller (BET) surface area as well as pore size distribution. As plotted in Fig. S3, FeN_4–Ru_6–NiN_4@PCA exhibited a huge specific surface

 https://doi.org/10.1007/s40820-026-02211-x

area of 472.32 $m^2 g^{-1}$ and a type-IV isotherm, indicating the coexistence of micropores and mesopores. The pore size distribution curve confirms the micro–mesopore domain structure of FeN_4–Ru_6–NiN_4@PCA, enhancing active site exposure and mass transfer during the ORR/OER process [24, 35]. The high-resolution transmission electron microscopy (HR-TEM) characterization data of the FeN_4–Ru_6–NiN_4@PCA catalyst (Fig. S4) indicate that there are no significantly disordered graphite layers in the porous carbon matrix. X-ray diffraction (XRD) patterns of PCA, FeN_4@PCA, FeN_4–NiN_4@PCA, and FeN_4–Ru_6–NiN_4@PCA (Fig. S5) display two diffusive reflections at ~ 26.2° and ~ 43.3°, corresponding to the (002) and (101) facets of the graphite lattice, respectively, without crystalline-phase peaks of Fe and Ni [36]. Furthermore, no crystalline-phase peak of Ru is detected, likely due to the small size (~ 2.5 nm) of the Ru nanoclusters (Fig. S6).

Raman spectroscopy (Fig. S7) reveals that FeN_4–Ru_6–NiN_4@PCA has an I_D/I_G ratio of 0.885, significantly lower than those of PCA (0.928), FeN_4@PCA (0.923), and FeN_4–NiN_4@PCA (0.895), indicating that the incorporation of FeN_4–NiN_4 dual sites and Ru clusters substantially enhances the graphitization of the carbon matrix. The highly graphitized structure of FeN_4–Ru_6–NiN_4@PCA promotes charge transfer and improves the durability of the carbon substrate against corrosion[16]. Figure 1e–g, S8 and S9 present the aberration corrected-high angle annular dark-field scanning TEM (AC HAADF-STEM) data of FeN_4–Ru_6–NiN_4@PCA in various selection fields, including ZIFs-derived carbon nanocage and CNTs, as well as the rGO. These images revealed that abundant isolated bright spots, corresponding to Fe/Ni SACs and several Ru NCs, are uniformly distributed on the carbon matrix. The HAADF-STEM image (Fig. 1h) and the energy-dispersive spectroscopy (EDS)-mapping data indicated a uniform distribution of C, N, Fe, Ni, and Ru species in the entire region of FeN_4–Ru_6–NiN_4@PCA, confirming the coexistence of isolated Ni and Fe atoms along with Ru NCs on the porous nitrogen-doped porous carbon aerogel [37].

X-ray absorption spectroscopic analyses were performed to determine the valence states and local atomic structures of the Fe, Ni, and Ru species in FeN_4–Ru_6–NiN_4@PCA. Reference spectra for Ni, Fe, and Ru foils, NiO, FeO, RuO_2, and nickel phthalocyanine (NiPc)/iron phthalocyanine (FePc) were also recorded for comparison. As depicted in Fig. 2a, the X-ray absorption near-edge structure (XANES) spectrum of FeN_4–Ru_6–NiN_4@PCA at Fe K-edge resembles those of FePc and FeO, indicating a cationic valence state for the Fe species in FeN_4–Ru_6–NiN_4@PCA. The Fe K-edge Fourier transformed-extended X-ray absorption fine structure (FT-EXAFS) spectrum of FeN_4–Ru_6–NiN_4@PCA shows a prominent peak at R = ~ 1.47 Å (Fig. 2d), similar to the Fe–N-related FT feature of FePc, suggesting the presence of an Fe–N coordination shell. Wavelet transform (WT) analysis was conducted on the EXAFS data to identify atomic arrangements in R- and k-spaces. In the Fe K-edge WT data for FeN_4–Ru_6–NiN_4@PCA (Figs. 2j and S10), a clear peak from the Fe–N bond is visible at ~ 6.5 $Å^{-1}$ in k-space, similar to that of FePc. The EXAFS fitting analysis (Fig. 2g and Table S1) demonstrated that the Fe–N coordination shell in FeN_4–Ru_6–NiN_4@PCA shows the coordination number of 3.94, highlighting that isolated Fe atom coordinates with four N ligands to form FeN_4 units.

As presented in Fig. 2b, the Ni K-edge XANES analysis indicated that the edge jump of Ni in FeN_4–Ru_6–NiN_4@PCA falls between that of Ni metal foil and $Ni^{2+}O$ reference, suggesting a positive valence state of the Ni species. The Ni K-edge energy in FeN_4–Ru_6–NiN_4@PCA closely matched that of the reference NiPc, implying similar oxidation states for the Ni cations in both materials. The EXAFS spectrum of FeN_4–Ru_6–NiN_4@PCA at Ni K-edge exhibited a prominent FT peak at R = ~ 1.44 Å (Fig. 2e), corresponding to the Ni–N bonding pair, similar to the Ni–N-related peak in NiPc, indicating exclusive coordination of Ni atoms with N atoms. Additionally, the WT contour data in Figs. 2k and S11 revealed a distinct peak related to the Ni–N coordination pair at ~ 7.5 $Å^{-1}$ for FeN_4–Ru_6–NiN_4@PCA, closely resembling NiPc, thus confirming Ni–N coordination. Curve-fitting analysis of the EXAFS data yielded the quantitative local structural parameters of FeN_4–Ru_6–NiN_4@PCA. As shown in Fig. 2h and Table S1, the Ni–N bonding pair in FeN_4–Ru_6–NiN_4@PCA has the coordination number of 3.81, indicating coordination of each isolated Ni atom with four N atoms, confirming the presence of Ni–N_4 moieties.

XANES analysis of the Ru K-edge showed a positive shift compared to that of the Ru foil (Fig. 2c). The FT-EXAFS spectrum of the Ru K-edge for FeN_4–Ru_6–NiN_4@PCA displayed a prominent peak at R = ~ 2.34 Å (Fig. 2f), nearly identical to that of the Ru foil. The WT analysis of the EXAFS data for FeN_4–Ru_6–NiN_4@PCA resembled that of the Ru foil (Fig. 2l). The EXAFS spectrum fitting analysis (Fig. 2i and Table S1) revealed that the coordination number

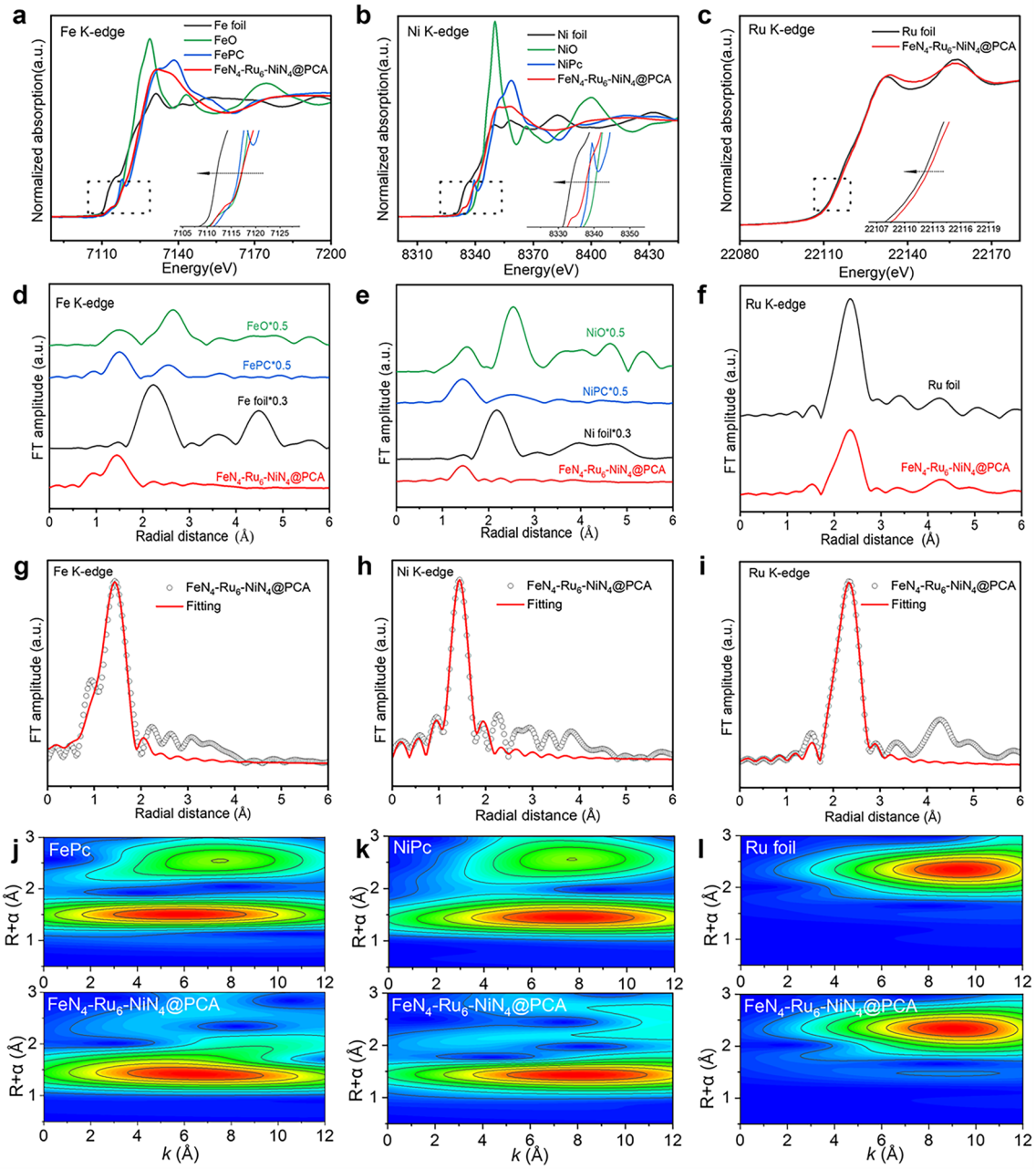

Fig. 2 Valence state and atomic local structure of FeN_4–Ru_6–NiN_4@PCA. **a–c** XANES, **d–f** FT-EXAFS, **g–i** Measured and fitted FT-EXAFS spectra, and **j–l** WT data of the k^3-weighted EXAFS spectra of FeN_4–Ru_6–NiN_4@PCA and the references

of Ru–Ru in FeN_4–Ru_6–NiN_4@PCA is 5.34, significantly lower than that of the Ru foil, indicating the presence of Ru_6 NCs. In summary, FeN_4–Ru_6–NiN_4@PCA was identified as a heterostructured catalyst with dual FeN_4/NiN_4 sites, in addition to Ru_6 NCs.

X-ray photoelectron spectroscopy (XPS) was utilized to characterize the surface elemental compositions and valence states of the synthesized materials. Figure S12 shows the full XPS survey spectra of FeN_4-Ru_6-NiN_4@PCA and FeN_4-NiN_4@PCA.As presented in Fig. S13, the Fe 2*p* XPS datum of FeN_4–Ru_6–NiN_4@PCA exhibits distinct peaks at 711.2 eV (Fe^{2+}),723.7 eV (Fe^{2+}), 713.6 eV (Fe^{3+}), and 726.9 eV (Fe^{3+}), confirming the absence of zero-valent Fe species [38]. Ni 2*p* XPS measurements on

 https://doi.org/10.1007/s40820-026-02211-x

FeN_4–Ru_6–NiN_4@PCA reveal peaks at 853.2 eV (Ni^{2+}) and 870.6 eV (Ni^{2+}), assigned as the Ni $2p_{3/2}$ and Ni $2p_{1/2}$ states of Ni cations, respectively (Fig.s S14) [39]. The N 1 *s* XPS data of FeN_4–Ru_6–NiN_4@PCA in Fig. S15 were deconvoluted into five components: pyridinic N (398.4 eV), metal–nitrogen (399.3 eV), pyrrolic N (400.3 eV), graphitic N (401.2 eV), and oxidized N (402.9 eV). The observation of a peak at 399.3 eV confirms the presence of Fe/Ni–N bonds in FeN_4–Ru_6–NiN_4@PCA [40]. Additionally, due to its low Ru content, no significant XPS signal of Ru was detected in FeN_4–Ru_6–NiN_4@PCA (Fig. S16). The inductively coupled plasma mass spectroscopy (ICP-MS) measurement was conducted to quantify the metal content in FeN_4–Ru_6–NiN_4@PCA. InTable S2, the contents of Fe, Ni, and Ru were 0.82, 0.74, and 0.39 wt%, respectively.

3.2 Oxygen Electrocatalyst Performance of FeN_4–Ru_6–NiN_4@PCA

The electrocatalytic ORR/OER activities of FeN_4–Ru_6–NiN_4@PCA were assessed using a standard three-electrode cell with a 0.1 M KOH electrolyte. Reference samples included PCA, FeN_4@PCA, FeN_4–NiN_4@PCA, as well as benchmark Pt/C and RuO_2 catalysts. All collected voltages were compared to that of reversible hydrogen electrode. In Fig. 3a, the linear sweep voltammetry (LSV) datum of FeN_4–Ru_6–NiN_4@PCA displays a high half-wave potential ($E_{1/2}$) of 0.874 V, outperforming Pt/C ($E_{1/2}$, 0.850 V), PCA (0.75 V), FeN_4@PCA (0.864 V), and FeN_4–NiN_4@PCA (0.860 V) [41]. As illustrated in Fig. 3b, the Tafel slope of FeN_4–Ru_6–NiN_4@PCA is 80 mV dec^{-1}, which is lower than those of Pt/C (92 mV dec^{-1}), PCA (104 mV dec^{-1}), and FeN_4–NiN_4@PCA (85 mV dec^{-1}), indicating faster ORR kinetics. Rotating ring-disk electrode measurements were conducted. In Fig. 3c, the H_2O_2 yield of FeN_4–Ru_6–NiN_4@PCA remains below 6.9% in the potential range of 0.3–0.9 V, with electron transfer numbers in the range of 3.86–3.99, suggesting that FeN_4–Ru_6–NiN_4@PCA follows a four-electron ORR reaction pathway. This finding aligns with the Koutecky–Levich (K–L) plots from LSV data at different rotation speeds (Fig. 3d) [42].

The ORR stability of FeN_4–Ru_6–NiN_4@PCA was assessed through a chronoamperometric (i–t) examination at a potential of 0.60 V. As displayed in Fig. 3e, FeN_4–Ru_6–NiN_4@PCA retained 96% of its initial current density after 12 h of ORR process. In contrast, FeN_4–NiN_4@PCA preserved 89% of its initial current, whereas Pt/C retained 86% under the same conditions. Morover, a slight negative shift in the polarization curves of FeN_4–Ru_6–NiN_4@PCA, corresponding to a 9 mV loss of $E_{1/2}$, is observed after 20,000 CV cycles (Fig. S17). In contrast, the $E_{1/2}$ degradation for Pt/C is 21 mV under the same conditons. These findings emphasize the outstanding stability of FeN_4–Ru_6–NiN_4@PCA during the ORR. This enhanced stability can be attributed to the significant coupling effect between the dual-atom sites and the NCs, which reduces demetallation of the metal sites and enhances the corrosion resistance of the carbon support. Furthermore, as depicted in Fig. 3f, FeN_4–Ru_6–NiN_4@PCA displayed remarkable methanol tolerance, sustaining a consistent current after methanol introduction in chronoamperometric i–t tests. In contrast, benchmark Pt/C exhibited a significant decline in current density after the methanol injection [43].

For OER, as depicted in Fig. 3g, FeN_4–Ru_6–NiN_4@PCA demonstrates a reduced potential of 1.58 V to reach a current density of 10 mA cm^{-2} ($E_{j=10}$), surpassing FeN_4–NiN_4@PCA ($E_{j=10}$, 1.63 V), FeN_4@PCA ($E_{j=10}$, 1.72 V), and PCA ($E_{j=10}$, 1.72 V). This highlights the significant role of Ru NCs in fostering a synergistic effect between FeN_4–NiN_4 dual sites and Ru clusters, thereby enhancing their OER performance. In addition, FeN_4–Ru_6–NiN_4@PCA exhibits a lower $E_{j=10}$ compared to commercial RuO_2 ($E_{j=10}$, 1.59 V), affirming its superior OER activity. The Tafel slope of FeN_4–Ru_6–NiN_4@PCA is 80 mV dec^{-1} (Fig. 3h), notably lower than PCA (145 mV dec^{-1}), FeN_4@PCA (122 mV dec^{-1}), FeN_4–NiN_4@PCA (94 mV dec^{-1}), and RuO_2 (89 mV dec^{-1}), demonstrating its enhanced OER kinetics. Additionally, as shown in Fig. 3i, the OER catalytic stability of FeN_4–Ru_6–NiN_4@PCA surpasses that of RuO_2. The FeN_4–Ru_6–NiN_4@PCA catalyst exhibits a minimal negative shift (11 mV) at $E_{j=10}$ after 3000 potential cycles (Fig. S18), further demonstrating its superior stability compared to RuO_2 under the same conditions. The overall bifunctional electrocatalyst functionality of FeN_4–Ru_6–NiN_4@PCA was evaluated by determining the difference between the $E_{j=10}$ for the OER and $E_{1/2}$ for the ORR, i.e., $\Delta E = E_{j=10} - E_{1/2}$. As plotted in Fig. 3j and Table S3, the ΔE value of FeN_4–Ru_6–NiN_4@PCA was 0.706 V, significantly lower than PCA ($\Delta E = 0.970$ V), FeN_4@PCA ($\Delta E = 0.856$ V), and FeN_4–NiN_4@PCA ($\Delta E = 0.770$ V). The bifunctional

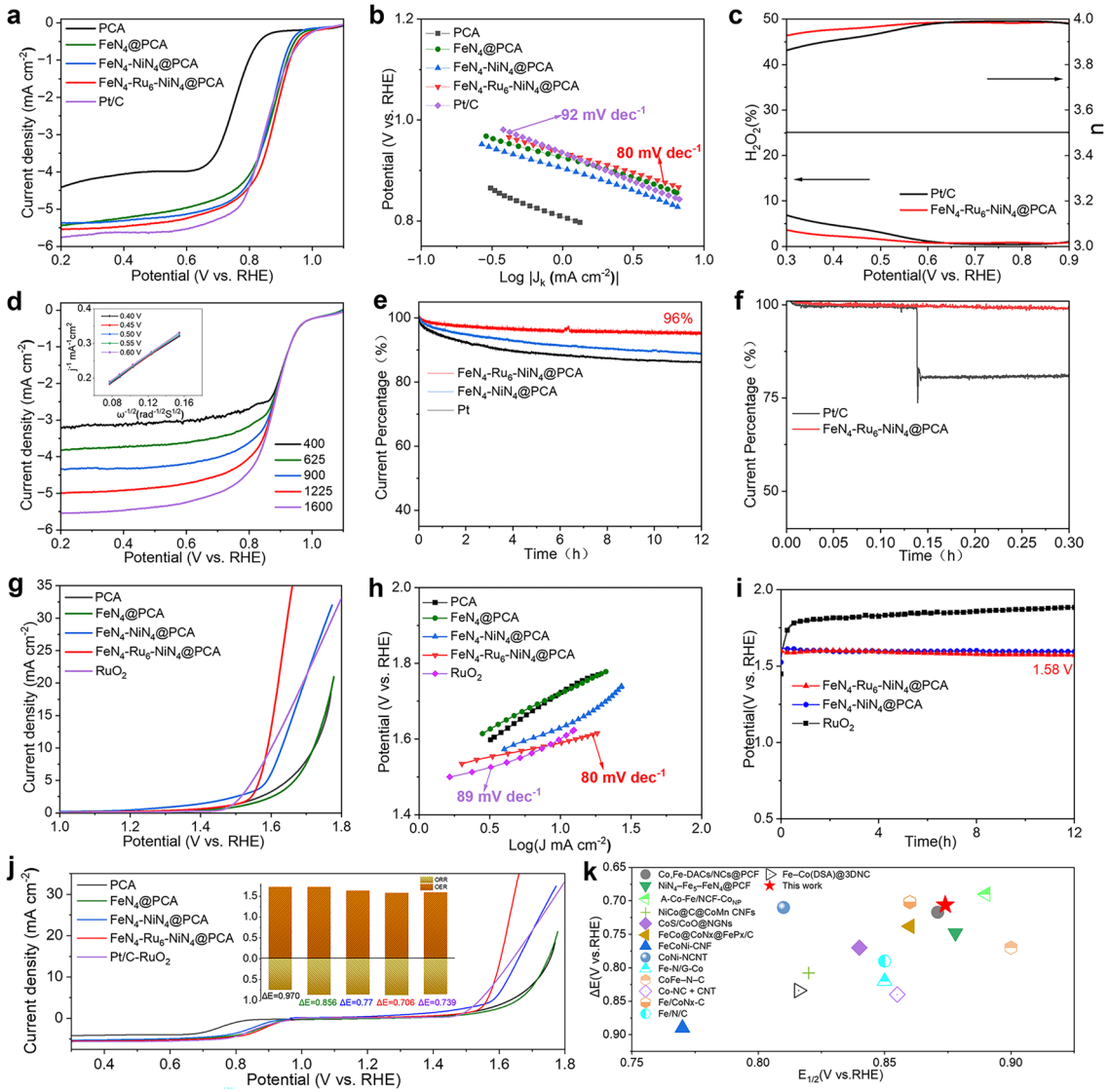

Fig. 3 Electrocatalytic ORR/OER performance and stability of FeN_4–Ru_6–NiN_4@PCA. **a** ORR-LSV curves at 1600 rpm for PCA, FeN_4@PCA, FeN_4-NiN_4@PCA, FeN_4–Ru_6–NiN_4@PCA, and Pt/C catalysts. **b** Tafel plots for FeN_4–Ru_6–NiN_4@PCA and the references. **c** H_2O_2 yield and electron transfer number (n) for FeN_4–Ru_6–NiN_4@PCA and Pt/C catalysts. **d** LSV data of FeN_4–Ru_6–NiN_4@PCA at various rotation speeds; inset presents the corresponding K–L plot. **e** Normalized chronoamperometry data of FeN_4–Ru_6–NiN_4@PCA, and Pt/C catalysts at 0.6 V vs. RHE. **f** Methanol tolerance curves of FeN_4–Ru_6–NiN_4@PCA and Pt/C catalysts during the chronoamperometric test. **g** OER-LSV curves at 1600 rpm for PCA, FeN_4@PCA, FeN_4–NiN_4@PCA, FeN_4–Ru_6–NiN_4@PCA, and Pt/C catalysts. **h** Tafel slopes for FeN_4–Ru_6–NiN_4@PCA and the references. **i** Chronopotentiometric curve of OER functionality of FeN_4–Ru_6–NiN_4@PCA, FeN_4–NiN_4@PCA, and RuO_2 at 10 mA cm^{-2}. **j** ORR-OER-LSV curves of FeN_4–Ru_6–NiN_4@PCA, and the references. **k** Comparison data of the $E_{1/2}$ and ΔE for FeN_4–Ru_6–NiN_4@PCA and other recently reported catalysts

oxygen catalytic performance of FeN_4–Ru_6–NiN_4@PCA is comparable to, or even superior to, that of the most recently reported SAC/DACs (Fig. 3k). Hence, the exceptional bifunctional electrocatalyst performance and durability of FeN_4–Ru_6–NiN_4@PCA position it as a promising candidate for renewable energy storage device applications [11, 44–46].

https://doi.org/10.1007/s40820-026-02211-x

3.3 Rechargeable ZAB Application of FeN_4–Ru_6–NiN_4@PCA

Given the outstanding ORR/OER functionalities of FeN_4–Ru_6–NiN_4@PCA, we evaluated its practical applicability in ZABs. An in-house aqueous ZAB was constructed using FeN_4–Ru_6–NiN_4@PCA deposited on carbon paper as the air cathode (see Figs. 4a and S19). For comparison, another ZAB was prepared by employing Pt/C + RuO_2 as a cathode catalyst. As depicted in Fig. 4b, the open-circuit voltage (OCV) of the FeN_4–Ru_6–NiN_4@PCA-based ZAB reaches 1.536 V, significantly higher than that of the Pt/C + RuO_2-based homolog (1.450 V). As presented in Fig. 4c, the FeN_4–Ru_6–NiN_4@PCA-based ZAB shows a reduced charge–discharge voltage gap compared with that of the Pt/C + RuO_2-based homolog, indicating its outstanding bifunctional ORR and OER performance in practical ZABs. The FeN_4–Ru_6–NiN_4@PCA-based ZAB achieved a peak power density of 197.76 mW cm^{-2}, which surpassed that of the Pt/C + RuO_2-based ZAB (173.2 mW cm^{-2}). Additionally,

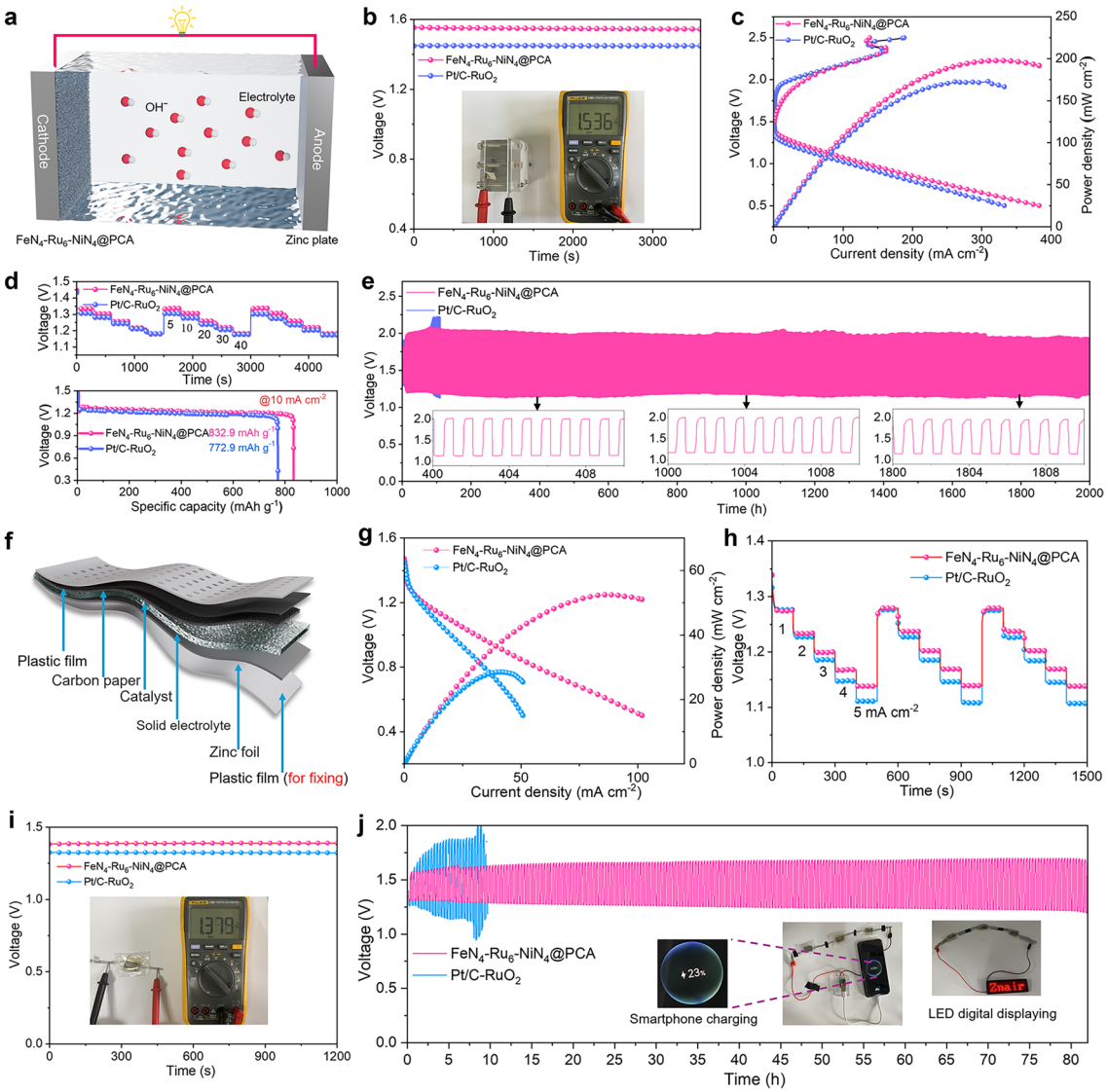

Fig. 4 Performance of ZABs with FeN_4–Ru_6–NiN_4@PCA as air cathode. **a** Scheme of liquid ZABs. **b** OCV (inset: OCV recorded by a multimeter), **c** polarization curves for charge–discharge and discharge power density, and **d** galvanostatic discharge curves of the ZABs at varying current densities (5–40 mA cm^{-2}) (top), specific capacity curves at 10 mA cm^{-2} (bottom). **e** Galvanostatic long-term cycling durability at 2 mA cm^{-2} for the assembled liquid ZABs. **f** Schematic diagram of the flexible solid-state ZABs. **g** OCV, **h** discharge polarization and power density curves, **i** current density-dependent galvanostatic discharge curves, and **j** constant current charge–discharge cycle performance of the flexible solid-state ZABs at 1 mA cm^{-2}

as illustrated in Fig. 4d (top), the FeN_4–Ru_6–NiN_4@PCA-based ZAB demonstrated improved discharge rate capability and stability at current densities ranging from 5 to 40 mA cm^{-2}. Moreover, the galvanostatic discharge specific capacity of the FeN_4–Ru_6–NiN_4@PCA-based ZAB was 832.9 mA h g^{-1} (Fig. 4d (bottom)), outperforming that of the Pt/C + RuO_2-based ZAB (772.9 mA h g^{-1}). To evaluate the cycling stability of FeN_4–Ru_6–NiN_4@PCA in ZABs, galvanostatic cycling tests were carried out at a current density of 2 mA cm^{-2} with 30 min of discharge and 30 min of charge. Impressively, the FeN_4–Ru_6–NiN_4@PCA-based ZAB demonstrated a minimal charge–discharge voltage gap and no noticeable voltage decay over 2000 h (Fig. 4e), indicating its exceptional long-term durability. In contrast, the charge–discharge potentials of the Pt/C + RuO_2-based ZAB decreased significantly after 95 h of cycling. As shown in Fig. S20, the performance of FeN_4–Ru_6–NiN_4@PCA-based ZAB competitively against those employing recently reported SACs/DACs [47–49]. These results emphasize the exceptional bifunctional oxygen electrocatalyst activity and stability of FeN_4–Ru_6–NiN_4@PCA in liquid ZABs [50]. Moverover, FeN_4–Ru_6–NiN_4@PCA also demonstrates outstanding structural robustness and stable chemical property after the cycling stability test, as evidenced by the TEM images in Fig. S21 and XRD pattern in Fig. S22.

Flexible solid-state ZABs were constructed by employing carbon paper loaded with FeN_4–Ru_6–NiN_4@PCA powder as the flexible air cathode, the polished zinc foil as the anode, and a flexible polyacrylamide (PAM) organohydrogel ternary hydrogel as the solid-state electrolyte (Fig. 4f) [51–53]. In Fig. 4g, the FeN_4–Ru_6–NiN_4@PCA-based flexible ZAB showed a higher OCV of 1.379 V than that of the Pt/C + RuO_2-based flexible ZAB (1.32 V). Additionally, the FeN_4–Ru_6–NiN_4@PCA-based flexible ZAB achieved a maximum power density of 53.4 mW cm^{-2}, surpassing that of the Pt/C + RuO_2-based flexible ZAB (Fig. 4h), and displayed excellent discharge rate performance at various current densities (1–5 mA cm^{-2}) (Fig. 4i). Notably, the flexible ZAB also exhibited stable cycle performance up to 80 h at 1 mA cm^{-2} (Fig. 4j). Furthermore, three serially connected solid-state flexible ZABs could power a mobile phone and an LED light (Fig. 4j, inset), showcasing their wide potential for practical energy storage applications [54]. Furthermore, the flexible ZABs based on FeN_4–Ru_6–NiN_4@PCA also exhibit good cycling stability at current densities of 2 and 5 mA cm^{-2} (Fig. S23).

3.4 Theoretically Elucidated Mechanism for Catalytic Activity of FeN_4-Ru_6-NiN_4@PCA

To gain an in-depth understanding the enhancement mechanism of Ru nanoclusters on the ORR/OER performance of FeN_4 and NiN_4 sites, we performed density functional theory (DFT) calculations. Based on the experimental data, we constructed two atomic models: FeN_4-Ru_6-NiN_4 and FeN_4-NiN_4 (Fig. 5a), in which FeN_4-Ru_6-NiN_4 represents the active site in FeN_4-Ru_6-NiN_4@PCA and FeN_4-NiN_4 acts as the active site in FeN_4-NiN_4@PCA. As shown in Fig. 5b, compared with FeN_4-NiN_4, FeN_4-Ru_6-NiN_4 exhibits a higher total density of states (TDOS) near the Fermi level, indicating enhanced electronic conductivity, which facilitates charge transfer during the ORR/OER processes. Both the ORR and OER proceed via a four-electron pathway involving the oxygen-containing intermediates of $*O_2$, *OOH, *O, and *OH (Figs. 5c and S24), where Fe and Ni centers serve as the active sites for ORR and OER, respectively.

As shown in Fig. 5d, the Gibbs free energy diagrams of the ORR on FeN_4 sites in both FeN_4-Ru_6-NiN_4 and FeN_4-NiN_4 demonstrate that all electron transfer steps occur spontaneously at zero potential (U = 0 V). At U = 1.23 V, the FeN_4 sites in FeN_4-Ru_6-NiN_4 exhibits the largest energy difference at the fourth reaction step ($*OH + e^- \rightarrow * + OH^-$), indicating that the desorption of *OH from the Fe centers is the rate-determining step (RDS). The free energy barrier of RDS for FeN_4-Ru_6-NiN_4 is calculated to be 0.519 eV, which is significantly lower than that for the FeN_4 sites in FeN_4-NiN_4 (0.574 eV), suggesting that FeN_4-Ru_6-NiN_4 species possesses thermodynamic advantages during the ORR. Furthermore, the charge density difference plots and Bader charge analysis of FeN_4 sites in FeN_4-Ru_6-NiN_4 and FeN_4-NiN_4 after O* absorption (Fig. 5f) demonstrates that the introduction of Ru_6 clusters induce electron redistribution and fewer electron transfer from Fe to O for OH*, which facilitates the OH* desorption at RDS. These results indicate that introducing Ru_6 nanoclusters in FeN_4-Ru_6-NiN_4@PCA effectively weakens OH* adsorption on the FeN_4 site, thus enhancing ORR kinetics.

We also conducted DFT calculations on NiN_4 sites in both FeN_4-Ru_6-NiN_4 and FeN_4-NiN_4 for the OER processes. As shown in Fig. 5e, at U = 0 V, the activation energy of the rate-determining step (RDS) of OER ($OH^- + * \rightarrow OH* + e^-$) at the FeN_4-Ru_6-NiN_4 is 1.948 eV, which is significantly lower than the 2.088 eV at the FeN_4-NiN_4. At U = 1.23 V, the

https://doi.org/10.1007/s40820-026-02211-x

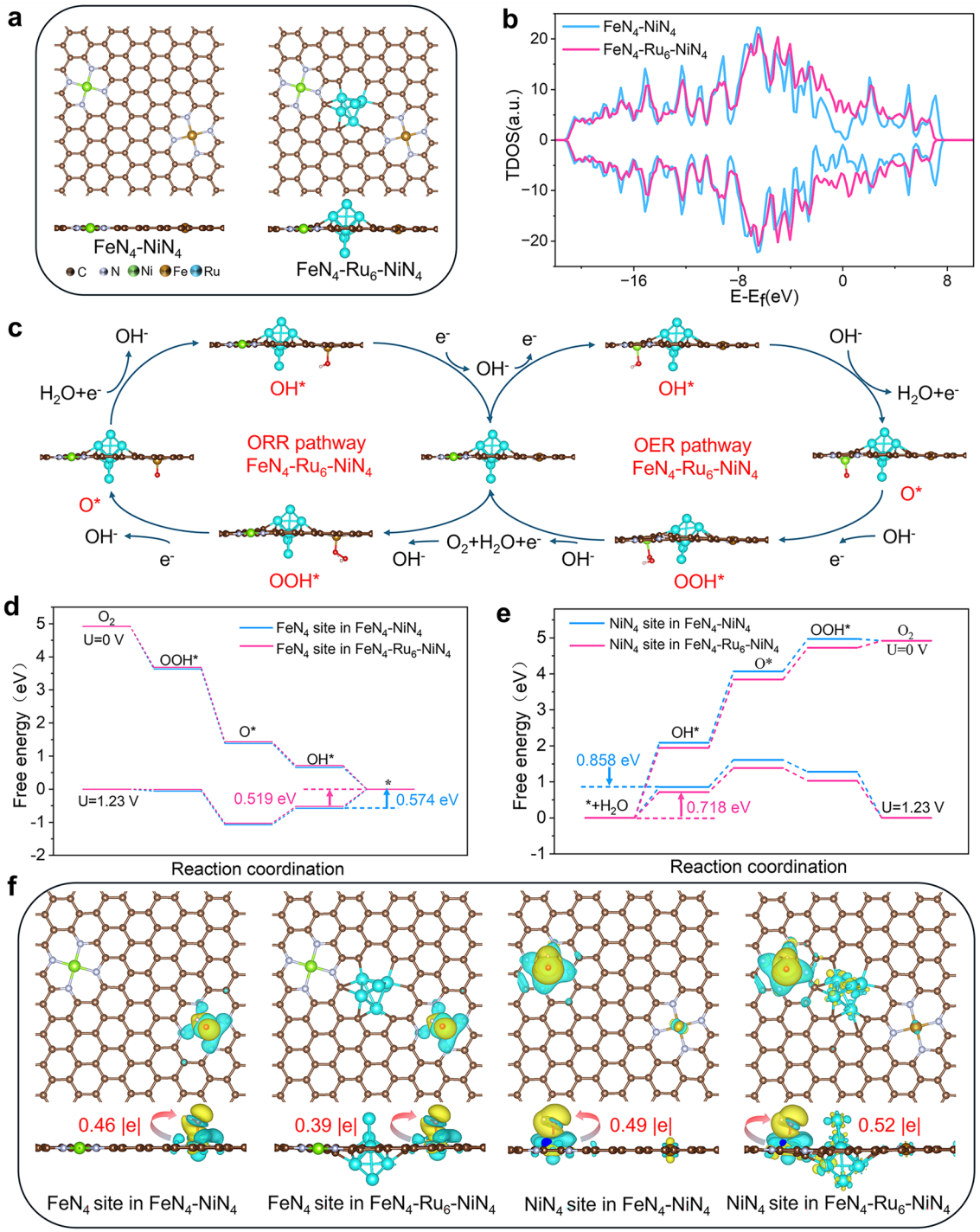

Fig. 5 DFT calculation results of ORR and OER performance for the FeN_4–Ru_6–NiN_4 and FeN_4–NiN_4. **a** Top and side views of three local atomic arrangements, **b** TDOS of FeN_4–NiN_4, and FeN_4–Ru_6–NiN_4 models. **c** Adsorption geometries along the ORR/OER pathway on the FeN_4 and NiN_4 sites in the FeN_4–Ru_6–NiN_4. **d** ORR free energy diagrams for FeN_4 sites in FeN_4–NiN_4 and FeN_4–Ru_6–NiN_4 at 0 and 1.23 V versus RHE. **e** OER free energy diagrams for NiN_4 sites in FeN_4–NiN_4 and FeN_4–Ru_6–NiN_4 at 0 and 1.23 V versus RHE. **e** Adsorption configurations at each key step on the FeN_4 and Ru@FeN_4 sites in the FeN_4–Ru_6–NiN_4@PCA model. **f** Charge density difference of FeN_4 and NiN_4 sites in FeN_4–Ru_6–NiN_4 and FeN_4–NiN_4 after OH adsorption (yellow contour: electron accumulation, blue contour: electron depletion)

maximum energy consumption at both the FeN_4-Ru_6-NiN_4 and FeN_4-NiN_4 sites also occurs at the first step. This indicates that the introduction of Ru_6 clusters adjacent to the NiN_4 sites can effectively reduce the reaction energy barrier and enhance the kinetics of the OER. Figure 5f shows the charge density difference distributions and Bader charge analysis results of NiN_4 sites in FeN_4-Ru_6-NiN_4 and FeN_4-NiN_4 after adsorbing the *OH intermediate. The results suggest that the presence of Ru_6 clusters in FeN_4-Ru_6-NiN_4 facilitate more electron (0.52 e) transferred from NiN_4 site to OH compared to that of FeN_4-NiN_4 (0.49 e), which enhances the interactions between the NiN_4 sites and OH and thus reduce the energy barrier of the RDS for OER processes. In summary, the Ru_6 clusters adjacent NiN_4 and FeN_4 sites effectively modulate their geometric/electronic structures, which facilitates the charge transfer and optimizes the adsorption–desorption behaviors of the key intermediates at RDSs, and ultimately enhances the ORR and OER kinetics.

4 Conclusions

In this study, we developed a porous carbon aerogel-supported heterogeneous catalyst containing atomically isolated dual NiN_4/FeN_4 sites associated with Ru_6 nanoclusters (FeN_4–Ru_6–NiN_4@PCA). Owing to the strong interactions between the Fe/Ni dual sites and Ru nanoclusters, FeN_4–Ru_6–NiN_4@PCA demonstrates exceptional ORR/OER activity and stability, achieving a high half-wave potential of 0.874 V for the ORR and a low potential of 1.58 V at 10 mA cm^{-2} for the OER, surpassing benchmark Pt/C and RuO_2 electrocatalysts. DFT calculations reveal that the Ru_6 clusters induce obvious electron redistribution of FeN_4/NiN_4 active sites, which optimize the electron transfer from the Fe/Ni to the key intermediate (*OH) at the RDSs, thus promoting the ORR/OER kinetics. Notably, aqueous ZABs utilizing FeN_4–Ru_6–NiN_4@PCA as the air cathode deliver a high peak power density of 197.76 mW cm^{-2} and stable cycling performance exceeding 2000 h (2000 cycles), significantly outperforming the ZAB with a Pt/C + RuO_2 air cathode. Furthermore, serially assembled flexible solid-state ZABs can charge mobile phones and power LED lights. This work presents an effective approach for developing highly active and robust bifunctional electrocatalysts coupling with dual-atom sites and nanoclusters for practical energy storage technologies.

Acknowledgements The authors would like to thank the finical support from the National Natural Science Foundation of China (52572253), the Basic Research Program in Natural Science Foundation of Jiangsu Province (BK20241923), and Science and Technology Guiding Plan Project of China National Textile and Apparel Council (2024031). This work was also supported by the National Natural Science Foundation of China (22369003), National Key Research and Development Program of China (No. 2021YFA1500800) and National Research Foundation of Korea (NRF) grant funded by the Korean government (MSIT) (RS-2023–00208355, RS-2024-00439825). The experiments at PAL were supported in part by MOST and POSTECH.

Author Contributions YZ conducted material synthesis and characterization, data curation and analysis, and original draft writing. KK performed some of the material characterization and data curation. HJ and YL conducted theoretical calculations and analysis. XJ and S-JH performed the XAS measurements and analysis. ZP was involved in review the draft writing. LL performed the final draft writing revision. ZW conceived and supervised the research and provided the funding acquisition and final draft writing revision. All authors contributed to discussions and manuscript review.

Declarations

Conflict of interest The authors declare no interest conflict. They have no known competing financial interests or personal relationships that could have appeared to influence the work reported in this paper.

Supplementary Information The online version contains supplementary material available at https://doi.org/10.1007/s40820-026-02211-x.

References

1. G. Nazir, A. Rehman, J.-H. Lee, C.-H. Kim, J. Gautam et al., A review of rechargeable zinc-air batteries: recent progress

and future perspectives. Nano-Micro Lett. **16**(1), 138 (2024). https://doi.org/10.1007/s40820-024-01328-1

2. S. Qiao, H. Shou, W. Xu, Y. Cao, Y. Zhou et al., Regulating and identifying the structures of PdAu alloys with splendid oxygen reduction activity for rechargeable zinc–air batteries. Energy Environ. Sci. **16**(12), 5842–5851 (2023). https://doi.org/10.1039/D3EE02719H
3. S. Chandrasekaran, R. Hu, L. Yao, L. Sui, Y. Liu et al., Mutual self-regulation of d-electrons of single atoms and adjacent nanoparticles for bifunctional oxygen electrocatalysis and rechargeable zinc-air batteries. Nano-Micro Lett. **15**(1), 48 (2023). https://doi.org/10.1007/s40820-023-01022-8
4. J. Zhang, Y. Yu, C. Zhu, D. Zhu, J. Li et al., Recent progress of carbon-based heterojunction electrocatalysts for zinc-air batteries. Coord. Chem. Rev. **549**, 217344 (2026). https://doi.org/10.1016/j.ccr.2025.217344
5. R. Liu, C. Jiang, J. Guo, Y. Zheng, L. Zhang et al., Activating Ru nanoclusters for robust oxygen reduction in aqueous wide-temperature zinc-air batteries. Matter **7**(11), 4031–4045 (2024). https://doi.org/10.1016/j.matt.2024.08.005
6. L. Lyu, X. Hu, S. Lee, W. Fan, G. Kim et al., Oxygen reduction kinetics of Fe–N–C single atom catalysts boosted by pyridinic N vacancy for temperature-adaptive Zn–air batteries. J. Am. Chem. Soc. **146**(7), 4803–4813 (2024). https://doi.org/10.1021/jacs.3c13111
7. Q. Kang, M. Su, Y. Luo, T. Wang, F. Gao et al., Chemical fermentation porecreation on multilevel bio-carbon structure with *in situ* Ni–Fe alloy loading for superior oxygen evolution reaction electrocatalysis. Nano-Micro Lett. **17**(1), 269 (2025). https://doi.org/10.1007/s40820-025-01777-2
8. Y. Chen, T. He, Q. Liu, Y. Hu, H. Gu et al., Highly durable iron single-atom catalysts for low-temperature zinc-air batteries by electronic regulation of adjacent iron nanoclusters. Appl. Catal. B Environ. **323**, 122163 (2023). https://doi.org/10.1016/j.apcatb.2022.122163
9. Z. Wang, Z. Lu, Q. Ye, Z. Yang, R. Xu et al., Construction of Fe nanoclusters/nanoparticles to engineer FeN_4 sites on multichannel porous carbon fibers for boosting oxygen reduction reaction. Adv. Funct. Mater. **34**(23), 2315150 (2024). https://doi.org/10.1002/adfm.202315150
10. Q. Ye, X. Yi, C.-Z. Wang, T. Zhang, Y. Liu et al., Data-driven screening of pivotal subunits in edge-anchored single atom catalysts for oxygen reactions. Adv. Funct. Mater. **34**(28), 2400107 (2024). https://doi.org/10.1002/adfm.202400107
11. P. Rao, Y. Yu, S. Wang, Y. Zhou, X. Wu et al., Understanding the improvement mechanism of plasma etching treatment on oxygen reduction reaction catalysts. Exploration **4**, 20230034 (2024). https://doi.org/10.1002/exp.20230034
12. Q. Chang, F. He, Z. Zhang, X. Fu, Y. Wang et al., Self-organized integrated electrocatalyst on oxygen conversion for highly durable zinc-air batteries. Angew. Chem. Int. Ed. **64**(4), e202416664 (2025). https://doi.org/10.1002/anie.202416664
13. B. Tang, Y. Zhou, Q. Ji, Z. Zhuang, L. Zhang et al., A Janus dual-atom catalyst for electrocatalytic oxygen reduction and evolution. Nat. Synth. **3**(7), 878–890 (2024). https://doi.org/10.1038/s44160-024-00545-1
14. J. Kundu, T. Kwon, K. Lee, S.-I. Choi, Exploration of metal-free 2D electrocatalysts toward the oxygen electroreduction. Exploration **4**(4), 20220174 (2024). https://doi.org/10.1002/EXP.20220174
15. Y. Li, Y. Li, H. Sun, L. Gao, X. Jin et al., Current status and perspectives of dual-atom catalysts towards sustainable energy utilization. Nano-Micro Lett. **16**(1), 139 (2024). https://doi.org/10.1007/s40820-024-01347-y
16. R. Xu, Z. Wang, X. Jin, T. Li, Z. Lu et al., NiN4/FeN4 dual sites engineered by Fe5 clusters on porous flexible carbon fibers for promoting oxygen reduction and evolution. J. Colloid Interface Sci. **693**, 137620 (2025). https://doi.org/10.1016/j.jcis.2025.137620
17. N. Liu, Y. Li, W. Liu, Z. Liang, B. Liao et al., Engineering bipolar doping in a Janus dual-atom catalyst for photo-enhanced rechargeable Zn-air battery. Nano-Micro Lett. **17**(1), 203 (2025). https://doi.org/10.1007/s40820-025-01707-2
18. L. Zhang, Y. Dong, L. Li, Y. Shi, Y. Zhang et al., Concurrently boosting activity and stability of oxygen reduction reaction catalysts *via* judiciously crafting Fe–Mn dual atoms for fuel cells. Nano-Micro Lett. **17**(1), 88 (2024). https://doi.org/10.1007/s40820-024-01580-5
19. Y. Li, H. Wang, C. Chen, X. Xie, Y. Yang et al., Ten thousand hour stable zinc air batteries *via* Fe and W dual atom sites. Nat. Commun. **16**, 8085 (2025). https://doi.org/10.1038/s41467-025-63540-w
20. H. Liu, J. Huang, K. Feng, R. Xiong, S. Ma et al., Reconstructing the coordination environment of Fe/co dual-atom sites towards efficient oxygen electrocatalysis for Zn-air batteries. Angew. Chem. Int. Ed. **64**(7), e202419595 (2025). https://doi.org/10.1002/anie.202419595
21. J. Qiao, Y. You, L. Kong, W. Feng, H. Zhang et al., Precisely constructing orbital-coupled Fe─Co dual-atom sites for high-energy-efficiency Zn–air/iodide hybrid batteries. Adv. Mater. **36**(32), 2405533 (2024). https://doi.org/10.1002/adma.202405533
22. W. Deng, Z. Song, M. Jing, T. Wu, W. Li et al., Highly active air electrode catalysts for Zn-air batteries: catalytic mechanism and active center from obfuscation to clearness. Carbon Neutralization **3**(4), 501–532 (2024). https://doi.org/10.1002/cnl2.133
23. J. Zhu, X.F. Lu, D. Luan, X.W.D. Lou, Metal–organic frameworks derived carbon-supported metal electrocatalysts for energy-related reduction reactions. Angew. Chem. Int. Ed. **63**(38), e202408846 (2024). https://doi.org/10.1002/anie.202408846
24. Z. Lu, Z. Wang, Z. Yang, X. Jin, L. Tong et al., Engineering CoN_4 and FeN_4 dual sites with adjacent nanoclusters on flexible porous carbon fibers for enhanced electrocatalytic oxygen reduction and evolution. Adv. Funct. Mater. **35**(16), 2418489 (2025). https://doi.org/10.1002/adfm.202418489
25. C. Zhao, B. Chu, H. Nian, B. Shao, Y. Lu et al., Sulfur-mediated microenvironment modulation of high-density Fe-N_4 sites for high-efficiency oxygen reduction and cryotolerant quasi-solid-state zinc-air batteries. Adv. Mater. **37**(47), e10621 (2025). https://doi.org/10.1002/adma.202510621

26. K. Yu, J. Qin, H. Zhang, S. Zhang, Y. Cao et al., Tailoring the first/second coordination layer of FeNi single atoms with nucleophile atoms to boost oxygen electrocatalysis for zinc-air batteries. Adv. Energy Mater. **15**(29), 2501091 (2025). https://doi.org/10.1002/aenm.202501091
27. T. Li, D. Zhang, Y. Zhang, D. Yang, R. Li et al., A pH-dependent microkinetic modeling guided synthesis of porous dual-atom catalysts for efficient oxygen reduction in Zn–air batteries. Energy Environ. Sci. **18**(10), 4949–4961 (2025). https://doi.org/10.1039/d5ee00215j
28. T. Qin, L. Zheng, Z. Pei, W. Wang, X. Ouyang et al., Electron redistribution *via* LDH-to-DACs coupling enhances d-band regulation and stability for zinc-air battery electrocatalysis. ACS Nano **19**(36), 32231–32245 (2025). https://doi.org/10.1021/acsnano.5c06786
29. Z. Qiu, T. Yang, P. Liu, Y. Zhang, X. Liang et al., Multidimensional interphase modulation by plasma for construction of advanced lithium metal batteries. Adv. Funct. Mater. **35**(42), 2501761 (2025). https://doi.org/10.1002/adfm.202501761
30. M. Shen, L. Xie, Y. Zhang, J. Sun, Y. Jia et al., Molecular engineering and channel structure modulation for single-atom iron-embedded high-porosity carbon fibers with enhanced oxygen reduction reaction and zinc-air battery performance. J. Colloid Interface Sci. **699**, 138230 (2025). https://doi.org/10.1016/j.jcis.2025.138230
31. L. Zhang, L. Zong, F. Lu, C. Wang, Z. Liu et al., Metal-saloph complexes pre-coordination for Fe single atom catalyst towards oxygen reduction reaction in rechargeable quasi-solid-state Zn-air battery. Appl. Catal. B Environ. Energy **370**, 125189 (2025). https://doi.org/10.1016/j.apcatb.2025.125189
32. H. Yu, C. Li, Y. Lei, Z. Xiang, Strategic secondary coordination implantation towards efficient and stable Fe─N─C electrocatalysts for the oxygen reduction reaction in PEMFCs. Angew. Chem. Int. Ed. **64**(33), e202508141 (2025). https://doi.org/10.1002/anie.202508141
33. M. Li, H. Chen, C. Guo, S. Qian, H. Li et al., Interfacial engineering on cathode and anode with iminated polyaniline@rGO-CNTs for robust and high-rate full lithium–sulfur batteries. Adv. Energy Mater. **13**(25), 2300646 (2023). https://doi.org/10.1002/aenm.202300646
34. J. Sun, M. Shen, A.J. Chang, J. Huang, P. Wang et al., Asymmetric Fe-N_3Se single atoms coupled with Fe atomic clusters on alveolar-inspired hierarchically porous carbon submicron-spheres for enhanced oxygen reduction. Appl. Catal. B Environ. Energy **383**, 126102 (2026). https://doi.org/10.1016/j.apcatb.2025.126102
35. J. Xu, Y. Meng, X. Qiu, H. Zhong, S. Liu et al., Honeycomb-like single-atom catalysts with FeN3Cl sites for high-performance oxygen reduction. Adv. Powder Mater. **4**(4), 100298 (2025). https://doi.org/10.1016/j.apmate.2025.100298
36. Y. Wu, S. Tang, W. Shi, Z. Ning, X. Du et al., Graphene-based phthalocyanine-assembled synergistic Fe-co-Ni trimetallic single-atomic bifunctional electrocatalysts by rational design for boosting oxygen reduction/evolution reactions. Carbon Energy **7**(9), e70062 (2025). https://doi.org/10.1002/cey2.70062
37. S. Xie, S. Tian, J. Yang, N. Wang, Q. Wan et al., Synergizing Mg single atoms and Ru nanoclusters for boosting the ammonia borane hydrolysis to produce hydrogen. Angew. Chem. Int. Ed. **64**(15), e202424316 (2025). https://doi.org/10.1002/anie.202424316
38. G. Qin, H.-G. Lu, G. Han, Y. Li, Ultrafast activity tuning and kilogram-scale synthesis of Fe–N–C catalysts *via* confinement-engineered joule heating. ACS Nano **20**(7), 6352–6363 (2026). https://doi.org/10.1021/acsnano.6c00048
39. L. Wu, M. Ning, X. Xing, Y. Wang, F. Zhang et al., Boosting oxygen evolution reaction of (Fe, Ni)OOH *via* defect engineering for anion exchange membrane water electrolysis under industrial conditions. Adv. Mater. **35**(44), 2306097 (2023). https://doi.org/10.1002/adma.202306097
40. J.-X. An, Y. Meng, L. Fang, Z. Lyu, S. Tang et al., Surface engineering strategy to synthesize bicomponent carbons for rechargeable zinc-air batteries. Energy Storage Mater. **70**, 103520 (2024). https://doi.org/10.1016/j.ensm.2024.103520
41. Y. Guo, Y. Xue, Z. Zhou, Revolutionizing Zn-Air batteries with chainmail catalysts: ultrathin carbon-encapsulated FeNi alloys on N-doped graphene for enhanced oxygen electrocatalysis. Chin. J. Catal. **58**, 206–215 (2024). https://doi.org/10.1016/S1872-2067(23)64603-0
42. L. Zhang, D.-H. Wu, M.U. Haq, J.-J. Feng, F. Yang et al., Coordination engineering and electronic structure modulation of FeNi dual-single-atoms encapsulated in N, P-codoped 3D hierarchically porous carbon electrocatalyst for synergistically boosting oxygen reduction reaction. Appl. Catal. B Environ. Energy **351**, 123991 (2024). https://doi.org/10.1016/j.apcatb.2024.123991
43. M.K. Kabiraz, J. Kim, H.J. Lee, S. Park, Y.W. Lee et al., Nickel nanoplates enclosed by (111) facets as durable oxygen evolution catalysts in anion exchange membrane water electrolyzers. Adv. Funct. Mater. **34**(46), 2406175 (2024). https://doi.org/10.1002/adfm.202406175
44. C. Kou, J. Zhou, H. Wang, J. Han, M. Han et al., Boron pretreatment promotes phosphorization of FeNi catalysts for oxygen evolution. Appl. Catal. B Environ. **330**, 122598 (2023). https://doi.org/10.1016/j.apcatb.2023.122598
45. Y. Guo, L. Yan, J. Li, J. Shi, Z. Liu et al., Zeolitic imidazolate framework induced CoFe-PBA/carbides hollow cube toward robust bi-functional electrochemical oxygen reaction. Chem. Eng. J. **472**, 144818 (2023). https://doi.org/10.1016/j.cej.2023.144818
46. W. Peng, S. Li, Y. Li, C.B. Musgrave III., B. Yuan et al., Breaking the limitations of activity and stability in powdered materials for oxygen evolution reaction: The critical role of catalyst-inducing seeds. Appl. Catal. B Environ. Energy **363**, 124777 (2025). https://doi.org/10.1016/j.apcatb.2024.124777
47. R. Xin, H. Zhao, Y. Liu, Y. Yuan, S. Liu et al., Homologous Mott–Schottky electrocatalysts enable record cycling stability in Zn-air battery and water splitting. Adv. Funct. Mater. **36**(27), e24205 (2026). https://doi.org/10.1002/adfm.202524205

 https://doi.org/10.1007/s40820-026-02211-x

48. H. Jiang, J. Xia, L. Jiao, X. Meng, P. Wang et al., Ni single atoms anchored on N-doped carbon nanosheets as bifunctional electrocatalysts for urea-assisted rechargeable Zn-air batteries. Appl. Catal. B Environ. **310**, 121352 (2022). https://doi.org/10.1016/j.apcatb.2022.121352
49. X. Zou, Q. Lu, J. Wu, K. Zhang, M. Tang et al., Screening spinel oxide supports for RuO_2 to boost bifunctional electrocatalysts for advanced Zn–air batteries. Adv. Funct. Mater. **34**(36), 2401134 (2024). https://doi.org/10.1002/adfm.202401134
50. S. Liang, L.-N. Song, X.-X. Wang, Y.-F. Wang, J.-Y. Wu et al., Fluid-induced piezoelectric field enhancing photo-assisted Zn–air batteries based on a Fe@P(V-T) microhelical cathode. Adv. Mater. **36**(44), 2407718 (2024). https://doi.org/10.1002/adma.202407718
51. X. Tang, Y. Wang, Z. Zhang, M. Xu, Z. Tao et al., Flexible Zn-air battery for self-powered aptasensing SARS-CoV-2. Nano Energy **127**, 109713 (2024). https://doi.org/10.1016/j.nanoen.2024.109713
52. J. Chen, C. Qiu, L. Zhang, B. Wang, P. Zhao et al., Wood-derived Fe cluster-reinforced asymmetric single-atom catalysts and weather-resistant organohydrogel for wide-temperature flexible Zn–air batteries. Energy Environ. Sci. **17**(13), 4746–4757 (2024). https://doi.org/10.1039/D4EE01226G
53. X. Fan, Y. Xie, Y. Jiao, P. Wu, Monodentate acetate anion enhanced hydrogel electrolyte for long-term lifespan Zn-air batteries. ACS Nano **18**(52), 35705–35717 (2024). https://doi.org/10.1021/acsnano.4c15570
54. J. Wang, S.-Y. Lang, Z.-Z. Shen, Y.-L. Zhang, G.-X. Liu et al., *In situ* visualization of interfacial processes at nanoscale in non-alkaline Zn-air batteries. Nat. Commun. **15**, 10882 (2024). https://doi.org/10.1038/s41467-024-55239-1